Applied Geochemistry 209 (2026) 107025

Contents lists available at ScienceDirect

Applied Geochemistry

journal homepage: www.elsevier.com/locate/apgeochem

Investigating iron–sulphur–phosphate transformation dynamics during redox-controlled microaeration of digested sludge towards improved resource recovery

Sophie Banke [a,b,*], Femke Deelstra [a], Thomas Prot [a], Leon Korving [a], Carlo Belloni [a], Iulian A. Dugulan [c], Mark C.M. van Loosdrecht [b]

[a] Wetsus, European Centre of Excellence for Sustainable Water Technology, Oostergoweg 9, Leeuwarden, 8911 MA, the Netherlands
[b] Department of Biotechnology, Delft University of Technology, Van der Maasweg 9, Delft, 2629 HZ, the Netherlands
[c] Department of Radiation Science and Technology, Delft University of Technology, Mekelweg 15, Delft, 2629 JB, the Netherlands

ARTICLE INFO

Editorial handling by: Elisa Sacchi

Keywords:
Phosphate removal
Iron speciation
Sulphur speciation
Iron(II)Oxyhydroxide
Sulphide oxidation
Digested sludge

ABSTRACT

Iron is an attractive binding partner for phosphorus removal from digested sludge, with recovery as the Fe(II) phosphate mineral vivianite ($Fe_3(PO_4)_2{\cdot}8H_2O$) representing a promising resource recovery pathway. However, sulphides compete strongly with phosphate for Fe(II), limiting vivianite formation and often requiring higher iron dosages. Because both iron and sulphur undergo redox transformations, controlled microaeration may alter the balance between iron sulphides, iron phosphates, and oxidized iron and sulphur species. This study investigated the effect of oxidation–reduction potential (ORP)-controlled microaeration (−220 to 0 mV) on Fe–S–P transformations in digested sludge. Microaeration showed contrasting effects. Mössbauer spectroscopy indicated an approximately 20% decrease in the Fe(II) associated with the vivianite fraction under all ORP conditions, while a pyrite-like iron sulphide phase remained largely unchanged. In contrast, the soluble phase showed increasing sulphur concentrations (ultimately recovered as sulphate) and a ~70% decrease in soluble phosphorus, suggesting enhanced iron–phosphate binding or adsorption during microaeration. Although the applied aeration conditions ultimately did not lead to vivianite formation, the proposed mechanism identifies an early microaeration window that favours phosphorus removal, providing a basis for further optimization of microaeration strategies for phosphorus recovery from anaerobic sludges.

1. Introduction

Vivianite ($Fe_3(PO_4)_2{\cdot}8\ H_2O$) has gained attention as a promising mineral for phosphate recovery from digested sludge due to its paramagnetic properties, which enable magnetic separation, a technique successfully demonstrated at pilot scale (Wijdeveld et al., 2022; Nguyen et al., 2024). This ferrous phosphate mineral typically forms under anaerobic conditions, as in the sludge digesters of wastewater treatment plants (WWTPs). Its low solubility and stability within a pH range of 6–8 favour its formation over other phosphate minerals, including calcium phosphates and struvite (Wilfert et al., 2018; Liu et al., 2018). The formation of vivianite is contingent upon the presence of iron, typically introduced via iron-based coagulants used in WWTPs for the removal of phosphate or sulphide, and to improve sludge dewatering (Wilfert et al., 2015). However, prior to phosphate precipitation, iron preferentially binds with sulphide due to the higher thermodynamic stability of iron sulphide species (Nriagu, 1972). This competitive interaction is well-documented in lake sediments, where vivianite formation is inhibited unless the molar ratio of reactive iron to sulphur remains above 0.9 (Rothe et al., 2015). Prot et al. (2020) (Prot et al., 2020) further demonstrated that vivianite can form in digested sludge when the Fe/S ratio is above 1. While lake sediments exhibit a range of FeS species—from amorphous phases to mackinawite ($Fe_{1+x}S$), greigite ($Fe^{2+}Fe_2^{3+}S_4$) and pyrite (FeS_2) (Lan and Butler, 2014)—crystalline forms such as pyrite are rarely observed in sludge environments (Prot et al., 2020; Amin et al., 2024; Wilfert et al., 2016). Since the iron sulphide composition is not well defined and difficult to analyze due to small particle size and low crystallinity, they are denominated FeS_x

* Corresponding author. Wetsus, European Centre of Excellence for Sustainable Water Technology, Oostergoweg 9, 8911 MA, Leeuwarden, the Netherlands.
E-mail addresses: sbanke@tudelft.nl (S. Banke), femke.deelstra@wetsus.nl (F. Deelstra), thomas.prot@wetsus.nl (T. Prot), leon.korving@wetsus.nl (L. Korving), carlo.belloni@wetsus.nl (C. Belloni), a.i.dugulan@tudelft.nl (I.A. Dugulan), M.C.M.vanLoosdrecht@tudelft.nl (M.C.M. van Loosdrecht).

https://doi.org/10.1016/j.apgeochem.2026.107025
Received 1 May 2026; Received in revised form 21 July 2026; Accepted 6 August 2026
Available online 7 August 2026

(Wilfert et al., 2016; Kubeneck et al., 2024; Mejia Likosova et al., 2013).

The preferential formation of iron sulphides necessitates additional iron dosing to enable subsequent vivianite precipitation, thereby increasing operational costs. For instance, assuming a sulphur content of 10 g S/kg dry weight (DW) (Wilfert et al., 2016) and an Fe/S ratio of 1, an additional 17 g/kg DW of iron must be dosed to satisfy sulphide binding before promoting vivianite precipitation. If iron sulphide formation could be suppressed, this additional iron could instead contribute directly to vivianite formation, potentially satisfying up to 19% of the required iron for phosphate precipitation in RWZI Nieuwveer, based on 38 g P/kg DW (Wilfert et al., 2016) and the stoichiometric vivianite Fe/P ratio of 1.5. One potential strategy involves the controlled oxidation of iron sulphides to liberate iron for vivianite formation. Ma et al. (2023) (Ma et al., 2023) demonstrated that vivianite can form from FeS via a dissolution–precipitation mechanism under conditions of continuous sulphide removal. An approach to remove sulphide involves oxidizing it to species such as elemental sulphur or sulphate, preventing the formation of the toxic H_2S gas. Pyrite oxidation is assumed to progress via an initial dissolution of the mineral producing iron(II) (Kirk Nordstrom, 1982; Moses and Herman, 1991), indicating a potential window for selective FeS destruction and vivianite formation. Although vivianite formation under such conditions has not yet been empirically demonstrated, the oxidation of iron sulphides in sludge has been investigated. Yin et al. (2021) (Yin et al., 2021) evaluated various oxidants and found that hydrogen peroxide (500 mg/L) was effective in controlling H_2S release, improving sludge dewaterability, and precipitating phosphate. However, the use of peroxides involves the use of chemicals and promotes Fenton-like reactions, increasing Fe(III) concentrations (Ismail et al., 2022). This can lead to the formation of ironhydroxyphosphates or oxidized iron (III) minerals such as ferrihydrite ($Fe_2^{3+}O_3 \cdot 0.5\ H_2O$) that are known to adsorb phosphate to a certain extent (WANG et al., 2015). Yet, the formation of vivianite would be more interesting, enabling both a more favorable Fe/P binding of 1.5 in comparison to the Fe(III) precipitates (van der Grift et al., 2016) as well as the magnetic recovery of iron and phosphate. Aeration presents a more promising alternative for iron sulphides oxidation, as it avoids the formation of radicals and is less environmentally aggressive compared to peroxides. Yin et al. (2021) (Yin et al., 2021) also explored aeration for sulphide removal but dismissed its application due to elevated H_2S production at pH ~6, which enhances H_2S volatility and increases pumping costs. Microaeration, in contrast, has attracted attention as a method for H_2S scavenging in anaerobic digestion systems (Chen et al., 2020). Microaerobic conditions are typically defined by oxidation-reduction potentials (ORP) between −230 and −180 mV (Chen et al., 2020; Krayzelova et al., 2015).

The primary objective of this research was to investigate an ORP-based controlled aeration in order to oxidize iron sulphides to Fe^{2+} and S^0, and the subsequent use of the iron for the formation of the Fe(II)-phosphate vivianite in digested sludge for more efficient phosphate recovery.

2. Material & methods

2.1. Digested sludge

Digested sludge was collected in April 2025 from RWZI Nieuwveer, and experiments were conducted from May to July of the same year. The composition of the digested sludge analyzed according to the procedure described in 2.3 is summarized in Table 1.

This characterized sludge composition is used as the reference initial condition for all experiments presented in this study. To ensure comparability, all experimental series were initiated from this common baseline composition, with sludge originating from the same homogenized sampling jerry can, stored at 4 °C and used within 2 months.

Table 1
Total elemental composition of microwave-digested sludge measured with ICP-OES and composition IC of the soluble fraction after 0.45 µm filtration, measured with ICP-OES and IC, including total solids (TS), volatile solids (VS), pH, and oxidation-reduction potential (ORP). Replicates are represented with N.

Elements/ Parameter	Total elements wet sludge (N = 3) *c* (g/kg)	Compounds	Composition soluble fraction(N = 2) *c* (mg/L)
Mg	210 ± 7	Mg	1.43 ± 0.05
P	1990 ± 40	P	116 ± 1
Fe	1580 ± 20	Fe	1.5 ± 0.4
S	630 ± 20	S	10 ± 1
Ca	1580 ± 10	Ca	56 ± 1
Al	330 ± 10	SO_4^{2-}	7 ± 3
TS	45.8 ± 0.2	K^+	250 ± 20
VS	29.4 ± 0.2	Na^+	110 ± 7
ORP (mV) (N = 1)	−350	Cl^-	143 ± 1
pH (N = 1)	8.7	NH_4^+ (N = 1)	3160
		HCO_3^- (N = 1)	5990

2.2. Aeration experiments

A total of 1.5 L of digested sludge was aerated under continuous stirring in the reactor system schematically depicted in Fig. 1. Both pH and oxidation–reduction potential (ORP) were regulated using limit switches, and all measurements were recorded via a data logger. A gas trap containing 0.01 M NaOH was installed to capture any H_2S potentially released during the experiments. Samples (15 mL) were withdrawn through an outlet at predefined intervals over 168 h (0, 3, 24, 48, 144, and 168 h). At the final sampling point, an additional 50 mL was collected for solids characterization.

To investigate the oxidative dissolution of iron sulphide, aeration was applied to maintain ORP setpoints of −220 mV, −150 mV, and 0 mV. These ORP targets were selected based on preliminary modelling using Visual MINTEQ, which used equimolar concentrations of iron, sulphur, and phosphorus at pH 7.8 as inputs. Mackinawite ($Fe_{1+x}S$) was selected as the representative iron sulphide phase, as it is hypothesized to be structurally similar to the initially forming FeS_x species (Rickard et al., 2006; Hu et al., 2020) Ferrihydrite was used to represent iron (III) oxyhydroxides, and vivianite was included as the relevant

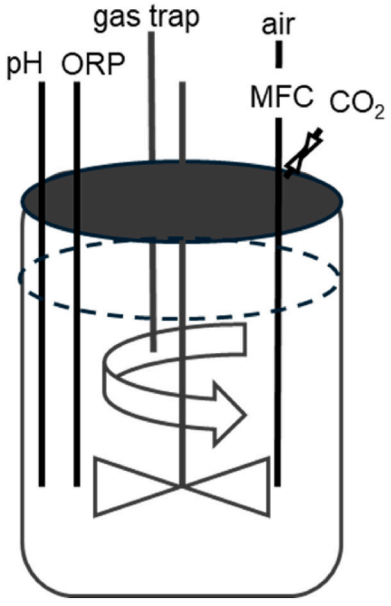

Fig. 1. Schematic of the reactor system used in aeration experiments, MFC = Mass flow control.

iron-phosphate mineral (Fig. 2). The thermodynamic predictions indicated that vivianite should dominate the iron mineralogy within an ORP window of approximately −250 mV to 0 mV. In addition to solid-phase predictions, aqueous Fe and S speciation was evaluated across the same redox range to support mechanistic interpretation.

During aeration, the pH increased to approximately 8.4, exceeding the typical optimum range for vivianite formation (pH 6–8) (Chen et al., 2022; Cao et al., 2019). Therefore, pH was controlled at 7.8 using CO_2 dosing. Hydrochloric acid was deliberately avoided based on prior laboratory observations that local acidic microenvironments created by HCl dosing may promote undesired vivianite dissolution. The temporal evolution of pH and ORP for all experimental conditions is presented in Figures A 1–3.

2.3. Characterization

2.3.1. Soluble components

For the analysis of the soluble fraction, samples were centrifuged at 4750 rpm for 10 min (Beckman Coulter Avanti J-15R). The supernatant was subsequently filtered through 0.45 µm syringe filters (Millipore). To minimize oxidation during filtration, the beaker headspace was continuously flushed with N_2. Elemental concentrations were quantified using inductively coupled plasma optical emission spectroscopy (ICP-OES; Thermo Scientific iCAP Pro). Ionic species were measured via ion chromatography (IC; Metrohm Compact IC Flex 88), and dissolved inorganic carbon (DIC) was determined using a total organic carbon analyzer (Shimadzu TOC-L CPH).

Evaporative losses resulted in sludge volume variations of up to 25% during the experiments. To correct for this, concentrations of soluble constituents were normalized using a correction factor (cf) derived from measured Na^+ and K^+ concentrations, which were assumed to remain constant throughout the experiment. The correction factor was calculated as:

$$cf = \left(\frac{c\,(Na^+)_t}{c(Na^+)_{0h}} + \frac{c\,(K^+)_t}{c(K^+)_{0h}} \right) \Big/ 2$$

where $c\,(Na^+)_{0h}$ and $c\,(K^+)_{0h}$ denote the initial sodium and potassium concentrations, and $c\,(Na^+)_t$ and $c\,(K^+)_t$ represent their concentration at time t.

2.3.2. Solid phase

The total elemental composition of the initial sludge was determined by microwave digestion of 2 mL wet sludge in 8 mL of 69% HNO_3, using a sludge-specific digestion protocol (180 °C, 15 min) on a Milestone Ethos Easy system, followed by ICP-OES analysis. In addition, both the initial sludge and the samples treated at −220, −150, and 0 mV were dried for one week under N_2 atmosphere in a glovebox (≤0.1% O_2). Subsequently, 50 mg of each dried sample were digested in 10 mL of 69% HNO_3 using the same microwave method. Solid-phase characterization comprised the following analyses:

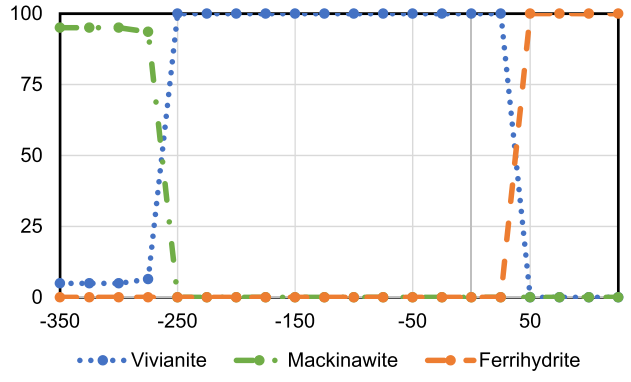

Fig. 2. Visual MINTEQ predictions for vivianite, mackinawite, and ferrihydrite distribution along different oxidation reduction potentials with Fe^{2+}, HS^-, PO_4^{3-} at equimolar concentrations of 10 mM, and pH fixed at 7.8.

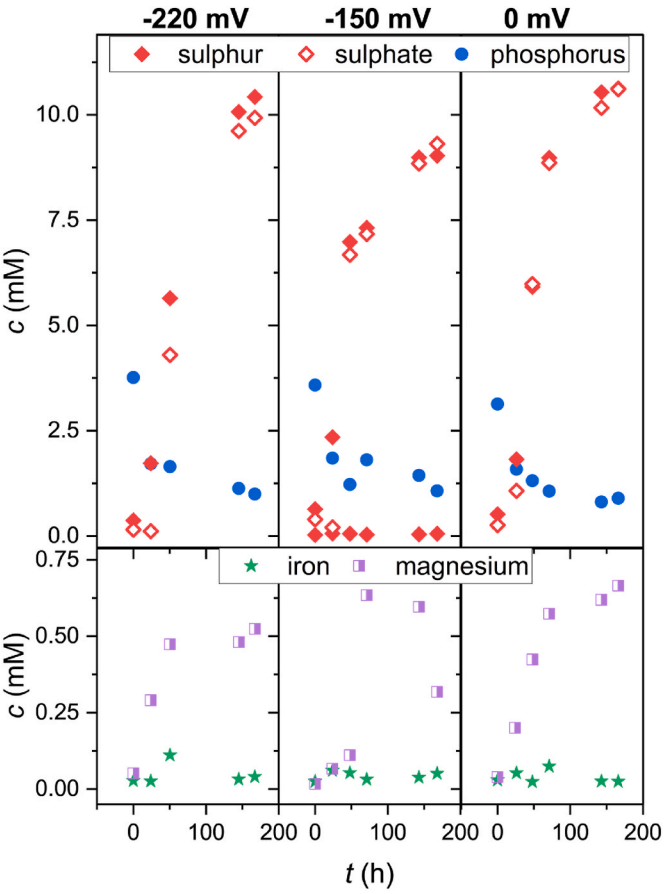

Fig. 3. Evolution of soluble sulphur, sulphate, and phosphorus concentrations, as well as soluble iron and magnesium concentrations during controlled aeration of digested sludge at three ORP levels.

- **Iron speciation:** Iron extractions were conducted by mixing 1 mL of sludge with 9 mL of 1 M HCl. Samples were shaken at 65 rpm for 4 h, filtered through 0.45 µm syringe filters under a continuous N_2 stream, and analyzed for Fe(II) and Fe(III) using a colorimetric assay (LCK 320, Hach Lange) (based on (Claff et al., 2010)).
- **Crystal phase determination:** X-ray diffraction (XRD) analysis (Bruker D8 Advance diffractometer) was used to identify crystalline phases. Powdered samples were mounted on Si510 wafers and scanned using Cu Kα radiation over 5°–80° 2θ with a step size of 0.008° and a dwell time of 2 s per step. Diffractograms were evaluated using Bruker DiffracSuite EVA software.
- **Iron mineral phase quantification:** Mössbauer spectroscopy was employed to quantify and speciate iron phases. Samples were dried, ground, and sealed under N_2 (≤0.1% O_2) in the glovebox prior to analysis. Measurements were performed using a conventional constant-acceleration or sinusoidal-velocity spectrometer equipped with a ^{57}Co(Rh) source and calibrated against α-Fe. Spectra were fitted using MossWinn 4.0 (Klencsár et al., 1996). Interpretation of Mössbauer spectra required differentiation among iron(III), low-spin (ls) Fe(II), and high-spin (hs) Fe(II) species. At room temperature, many iron-bearing compounds appear as paramagnetic (pm) doublets due to superparamagnetic behaviour or their electronic configuration. Some phases become magnetically ordered below their Curie or Néel temperatures and are thus observed as sextets or

octets—for example, vivianite forms antiferromagnetic (afm) octets below its Néel temperature (Meijer et al., 1967).

- **4 K measurements:** Spectra acquired at 4 K provide the most accurate quantification (Murad and Cashion, 2004). However, at this temperature, more phases become magnetically ordered, increasing spectral complexity.
- **20 K measurements and vivianite fitting:** To maintain vivianite in its paramagnetic state, measurements were also conducted at 20 K, above its Néel temperature of 12 K (Meijer et al., 1967), while minimizing temperature-related noise. Paramagnetic vivianite is characterized by two hs-Fe(II) doublets with isomer shifts (IS) of approximately 1.3 mm s^{-1} and quadrupole splittings (QS) of ~2.6 mm s^{-1} and ~3.2 mm s^{-1} (at 77 K; Dyar et al., 2014), corresponding to the A and B crystallographic sites. The expected A/B intensity ratio of ~0.5 reflects the structural occupancy of vivianite (Grodzicki and Amthauer, 2000). Deviations from this ratio may indicate Fe(II) oxidation, substitution by other cations such as Mg^{2+} (Kubeneck et al., 2023), or overlapping spectral contributions.
- **Distinguishing low-spin Fe(II) from Fe(III):** Low-spin Fe(II) in iron sulphides, common in digested sludge (Wilfert et al., 2016), typically overlaps with pm-Fe(III) doublets. Most iron sulphides observed in sludge, including thermodynamically stable pyrite (Thompson et al., 2025), remain paramagnetic at 4 K, facilitating their distinction from magnetically ordered Fe(III).
- **Fe(III) in vivianite versus other Fe(III) phases:** Fe(III) within oxidized vivianite is expected to become magnetically ordered at the same Néel temperature as Fe(II) in vivianite. Thus, Fe(III) appearing as a paramagnetic doublet at 20 K but as an afm sextet at 4 K may be indicative of oxidized vivianite.
- **Green rust identification:** Green rust, a mixed-valence Fe(II)–Fe(III) double-layer hydroxide with intercalated anions ($[Fe(II)_{1-x}Fe(III)_x(OH)_2]^{x+}\cdot[(x/n)A^{n-}\cdot(m/n)H_2O]^{x-}$, where $A^{n-} = CO_3^{2-}$, SO_4^{2-}, Cl^-, OH^-) (Thompson et al., 2025), has recently been reported to form in aquatic sediments as an alternative to vivianite (Kubeneck et al., 2025). Evidence of green rust presence was also observed in the present samples (Text A 1, Figure A 4).

3. Results & discussion

3.1. Microaeration to −220 mV is sufficient to increase sulphur and decrease phosphorus concentrations in solution

Across all aeration experiments, sulphur species were released into the liquid phase, as quantified by ICP-OES, with release rates slowing after approximately 72 h (Fig. 3). The 0 mV treatment exhibited the highest overall sulphur release. Interestingly, the −220 mV experiment showed a higher release than the −150 mV experiment. While this may initially appear counterintuitive, it can be explained by the actual ORP evolution during the experiments (Figure A 1-3). For approximately the first 24 h, all systems remained close to −250 mV, after which the −150 mV condition increased more rapidly towards its setpoint, whereas the −220 mV and 0 mV treatments followed more similar ORP trajectories during the first ~48 h. As a result, these two systems experienced comparable redox environments over a substantial portion of the experiment, which likely contributed to their similar sulphur release behaviour. Throughout the experiments, measured sulphur and sulphate concentrations were closely aligned, indicating that sulphate was the predominant dissolved sulphur species. During the first 24 h, however, sulphate concentrations were notably lower—particularly under more reducing conditions—suggesting the transient presence of other sulphur species. Thiosulphate concentrations were below the detection limit and therefore cannot account for this discrepancy. A plausible explanation is the formation of elemental sulphur particles smaller than 45 μm. In wastewater systems, biological oxidation of sulphides to elemental sulphur has been reported to proceed more rapidly than chemical oxidation to sulphate or thiosulphate (Nielsen et al., 2006). Thus, the initial formation of fine elemental sulphur particles could explain the temporarily lower sulphate concentrations observed in the first 24 h.

In addition to sulphide oxidation and dissolution, a net decrease of approximately 70% in soluble phosphorus was observed, indicating substantial phosphorus precipitation. Soluble Fe (Fig. 3) increased during the first 48 h—most notably at −220 mV. The evolution of soluble Fe, S and P supports an early FeS_x dissolution with transient Fe release coinciding with both sulphur mobilization and the rapid initial decrease in dissolved phosphorus. Thermodynamic modelling of aqueous Fe and S speciation across the investigated redox range provides further support for this interpretation (Figure A 4). The simulations indicate that dissolved S(−II) species decrease by several orders of magnitude with increasing ORP, coinciding with the oxidation observed under the applied aeration conditions in the laboratory. In contrast, Fe(II) remains comparatively stable, with only minor changes in concentration, in contrast to the small spike measured with ICP. These observations suggest that sulphide oxidation proceeds as predicted by thermodynamics, but iron dissolution could be influenced by kinetic factors.

Kinetic factors could provide additional insight into the differences in soluble phosphorus removal, although their interpretation should be treated with caution due to the irregular ORP evolution across reactor runs, which limited reproducibility. Nevertheless, all reactors exhibited a similar initial phase during the first 48 h, characterized by a rapid decrease in soluble phosphorus of approximately 70%. Beyond 48 h, phosphorus removal slowed markedly under the −220 and 0 mV conditions, with a slight increase in soluble phosphorus observed at the end of the 0 mV experiment. In contrast, the −150 mV condition showed an earlier increase in soluble phosphorus after approximately 24 h, followed by a slight decline. The −220 mV experiment, which remained at low ORP for the longest period, exhibited the steepest phosphorus decline, coinciding with the highest soluble Fe concentration. This suggests that prolonged exposure to lower ORP promoted iron-mediated phosphorus removal, whereas transient increases in soluble phosphorus were associated with the higher ORP conditions.

To relate the extent of sulphur release to phosphorus removal, the ΔS/ΔP molar ratio was calculated for each experimental condition (Table 2). Ratios were 3.6 and 3.3 for −220 mV and −150 mV, respectively, and 4.5 for 0 mV. The elevated value of −220 mV relative to −150 mV may again reflect the aforementioned ORP overshoot. Following the Fe/S binding ratio of approximately 1 reported for sludge (Prot et al., 2020), as previously introduced, a 1/1 dissolution of Fe and S was assumed when constructing Fe/P binding scenarios. Precipitation of phosphate with Fe(II) would likely result in vivianite formation, which exhibits a Fe/P molar ratio of 1.5. In contrast, Fe(III) and phosphate commonly form iron hydroxyphosphates with Fe/P ratios ranging from 1.7 to 2 under neutral pH conditions (van der Grift et al., 2016). The observed ΔS/ΔP ratios (>2) therefore align more closely with the stoichiometry associated with iron hydroxyphosphate formation. However, this interpretation is based exclusively on liquid-phase measurements, whereas solid-phase mineralogy also plays a crucial role in determining phosphorus binding stoichiometry. The amount of iron liberated to bind phosphate depends on the specific sulphide and iron species present initially. Furthermore, phosphate previously incorporated in struvite (as confirmed by XRD; Figure A 7) may have undergone cation exchange or re-precipitation, supported by the slight release of magnesium into solution (Figure A 6).

3.2. Microaeration leaves pyrite-like Fe(II) phase intact but oxidizes other Fe(II) phases

The initial, unaerated sample, measured at −350 mV ORP, was first characterized to establish the baseline iron speciation for comparison with the microaerated reactors. The Mössbauer spectra (Fig. 4) were

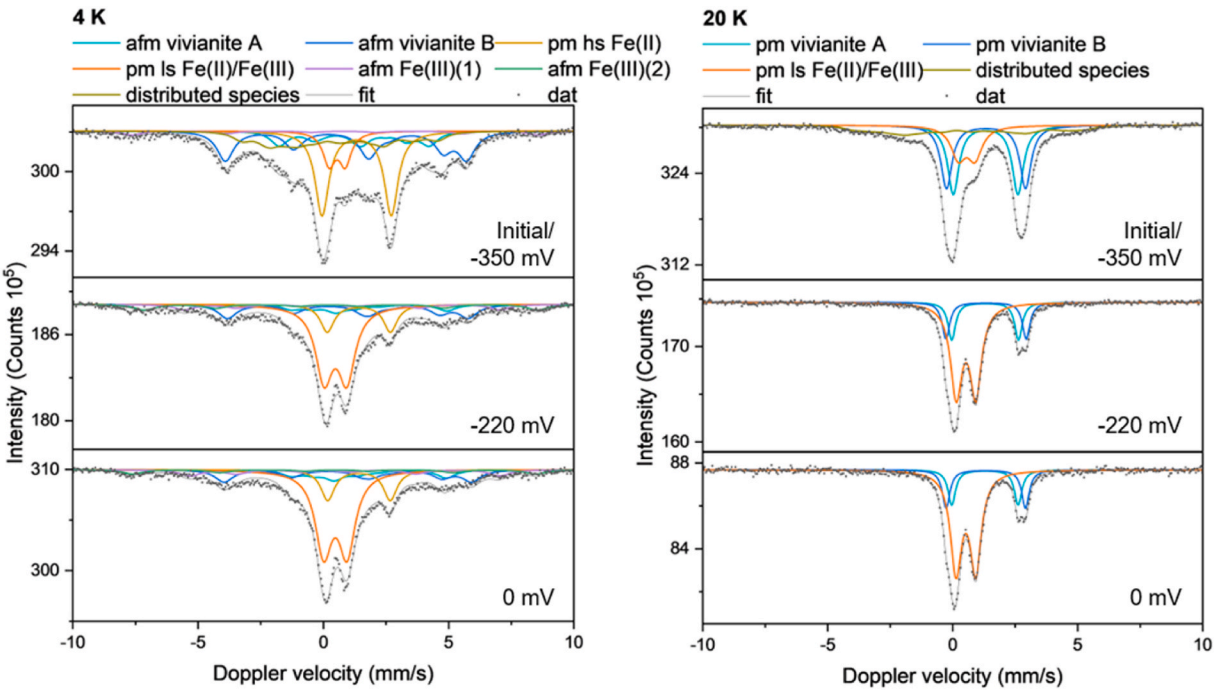

Fig. 4. Mössbauer spectra at 20 K and 4 K of initial sludge, and sludge oxidized at on ORP of −220 mV, and 0 mV sludge samples with fitted iron phases. afm = antiferromagnetic; pm = paramagnetic; ls = low spin; hs = high spin.

Table 2
Change of total amount of sulphur species (ΔS) and phosphorus (ΔP) in solution and the ΔS/ΔP ratio for each digested sludge experiment shown in Fig. 3.

	concentration (mM)		
	−220 mV	−150 mV	0 mV
ΔS (increased in solution)	10.1	8.3	10.0
Δ P (decreased in solution)	2.8	2.5	2.2
ΔS/ΔP	3.6	3.3	4.5

interpreted according to the approach described in Section 2.3 and detailed further in Text A1. At 20 K, two Fe(II) sites attributable to vivianite (sites A and B, light and dark blue) were identified, together with low-spin Fe(II)/Fe(III)-containing phases (orange) and a distributed spectral component that may also originate from FeS-derived species (green-gold). Additional discrimination between the low spin Fe(II) and Fe(III) phase (orange) was obtained from the 4 K spectra. At this temperature, the low-spin Fe(II)/Fe(III) component of the unaerated sample was most likely associated with a pyrite-like (FeS_2) phase, the relative abundance of which (approximately 10%, Table A 1) is consistent with the non-extractable iron fraction determined by sequential extraction (Fig. 5). For the green-gold contribution a fit was a magnetically distributed fit was attempted at 20 K (Table A 1). Previous studies have shown that FeS_x minerals can exhibit irregular magnetic ordering and poorly defined Mössbauer signatures (Kubeneck et al., 2024; Thompson et al., 2025), complicating spectral deconvolution. Although the QS parameter obtained here (IS = 0.40 mm/s, QS = 0.51 mm/s, B = 21 T at 21 K, Table A 1) does not fully align with literature values (IS = 0.40 mm/s, QS = 0.13 mm/s, B = 17-20 T at 77 K) (Kubeneck et al., 2023), the observed irregularity could indicate the presence of a FeS_x species.

Changes in vivianite content were assessed by tracking the spectral area of the vivianite B site at 20 K (Text A 1). Aeration resulted in a reduction of the B-site contribution by 22% (from 29% initially to 17% in the −220 mV and 0 mV treatments compared to the initial sample), indicating that microaeration led to partial oxidation or degradation of

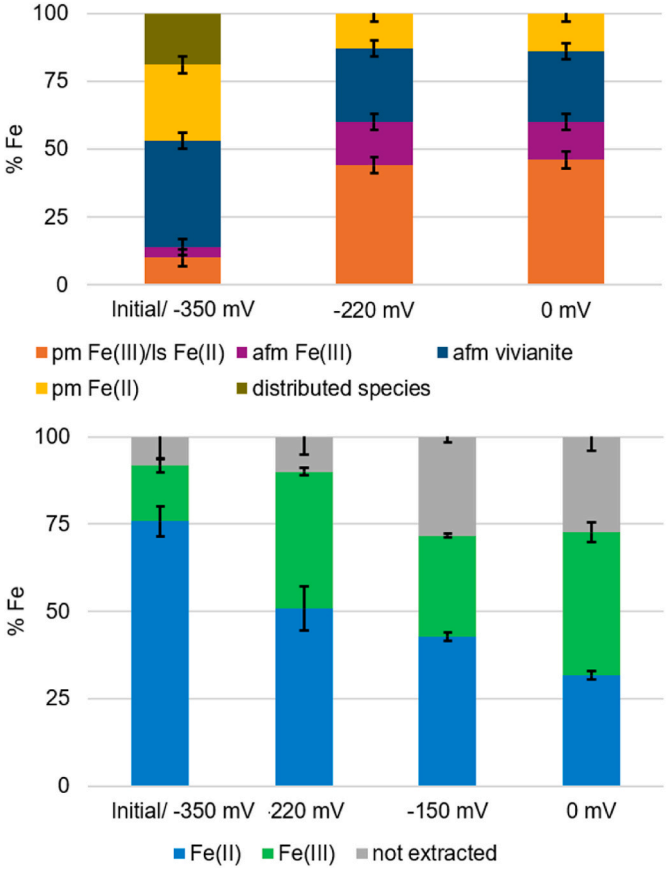

Fig. 5. % Fe in different iron phases as per 4 K Mössbauer spectroscopy (top) and HCl extraction (bottom). afm = antiferromagnetic; pm = paramagnetic; ls = low spin; hs = high spin.

vivianite. To evaluate whether this loss originated from vivianite

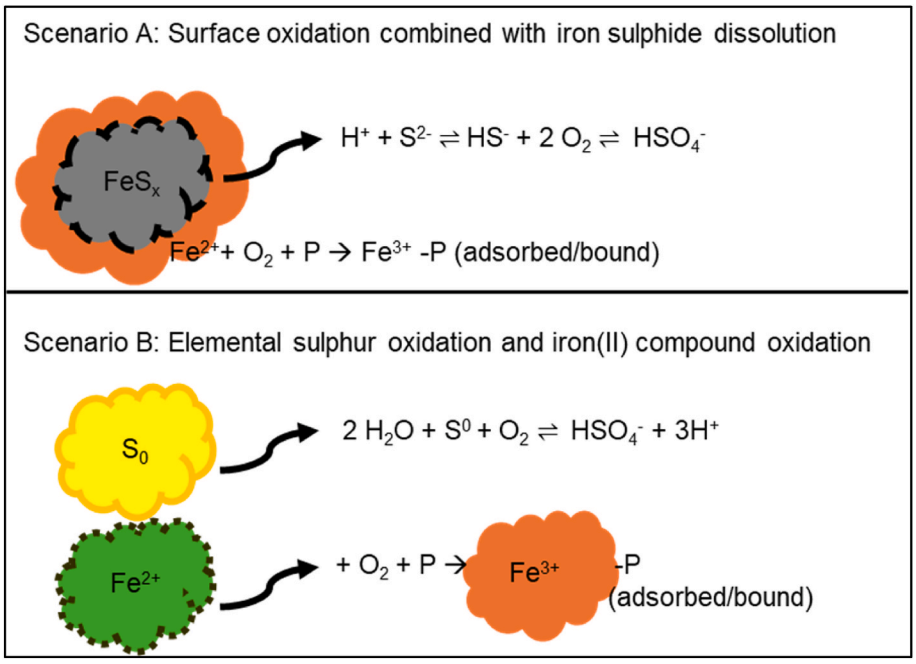

Fig. 6. Scenarios for iron and sulphur species that could react upon oxidation and provoke phosphorus decrease in the solution.

oxidation, the increase in antiferromagnetically ordered (afm) Fe(III) between 20 K and 4 K was examined. Magnetic ordering below 20 K is expected for Fe(III) within vivianite or green rust (Section 2.3, Text A 1). Only an increase of 10–12% afm Fe(III) was detected in the −220 mV and 0 mV samples. Even if this entire increase were attributed to oxidized vivianite rather than Fe(III) present in green rust, it would correspond to only a small fraction of the total reduction in vivianite B-site signal. Thus, another portion (10–12%) of originally crystalline Fe (II)-vivianite was converted into non-magnetically ordered iron (III) phases, demonstrating that microaeration induces both oxidation and structural breakdown of vivianite.

The fraction of Fe(II)-vivianite not transformed into afm Fe(III) was likely detected as paramagnetic (pm) low-spin (ls) Fe(II)/Fe(III). This pm contribution (orange doublet at 4 K) increased considerably in both microaerated samples. This increase is attributable not only to vivianite alteration but also to oxidation of a pm high-spin (hs) Fe(II) phase (yellow doublet at 4 K). Notably, this pm hs Fe(II) partially overlaps with the pm signal of vivianite site A, complicating precise deconvolution of vivianite and green rust-like phases (Text A 1, Figure A 5). The presence of paramagnetic phases at 4 K may be due to very small particle sizes (<30 nm) or lattice disorder—both conditions known to suppress magnetic ordering (Thompson et al., 2025). Such disorder may arise from impurities within vivianite crystals (Wilfert et al., 2016). Alternatively, these pm signatures could originate from green rust, which may remain incompletely magnetically ordered even at 4 K (Notini et al., 2023). In summary, microaeration converted both (i) part of the afm Fe(II)-vivianite and (ii) the pm hs Fe(II) phases—originating either from nanocrystalline/impure vivianite or from green rust—into pm Fe (III). This demonstrates that microaeration promotes broad oxidation processes affecting multiple Fe-bearing mineral phases.

The quantification of iron sulphiedes was considerably complicated by the presence of paramagnetic (pm) Fe(III) at 4 K, as the pm Fe(III) signal continued to overlap with the low-spin (ls) Fe(II) contribution (orange component). XRD analysis did not resolve the iron sulphide phases either, indicating that these phases lacked sufficient crystallinity for detection (Figure A 7). To assess whether microaeration led to the destruction of iron sulphides, changes in other Mössbauer-assigned iron fractions, particularly antiferromagnetic (afm) vivianite and pm high-spin (hs) Fe(II), were therefore interpreted. Fig. 5 (top) summarizes the evolution of five key spectral contributions between the initial and microaerated samples: afm vivianite (blue), pm hs Fe(II) (yellow), afm Fe(III) (purple), ls Fe(II)/Fe(III) (orange), and a species with a magnetically distributed fit (gold-green), only in the initial sample. Assuming the orange contribution in the initial sample at 4 K was derived from iron sulphide only as argued above, the iron sulphide content in the microaerated samples was estimated using:

$$\text{ls Fe(II)} = \Delta\text{orange} - \Delta\text{gold-green} - \Delta\text{yellow} - (\Delta\text{blue} - \Delta\text{purple})$$

The resulting estimates 9 ± 9% for the −220 mV sample and 10 ± 9% for the 0 mV sample carry substantial uncertainty due to the cumulative 3% fitting uncertainty for each spectral component. Despite the large error margins, these values are similar to the 9% ls Fe(II) measured in the initial sample, suggesting that the iron sulphide fraction likely remained largely intact during microaeration. Thus, the influence of aeration on iron sulphide oxidation appears limited. Nevertheless, the potential FeSx species observed in the initial sample at 20 K was not present in the aerated samples. This would indicate this potential second FeSx phase was more labile to aeration and would be thus more interesting for iron sulphide transformations.

The combined analyses clearly demonstrate that microaeration leads to substantial oxidation and structural alteration of vivianite and other mixed Fe(II)/Fe(III) phases such as green rust. In contrast, the ls Fe(II) iron sulphide fraction appears resistant to oxidation under the conditions tested. This raises important questions regarding the nature of the iron and sulphur phases in the initial sludge and the mechanisms by which sulphur was mobilized, and phosphorus was removed from solution.

3.3. *Mechanistic scenarios for Fe–S–P transformations during microaeration*

The results show that microaeration promoted sulphide oxidation, as reflected by the increase in dissolved sulphur that ultimately accumulated as sulphate, while simultaneously decreasing soluble phosphorus concentrations and oxidizing Fe(II)-bearing mineral phases, including vivianite. Consequently, the intended objective of promoting net vivianite formation was not achieved under the applied aeration conditions, suggesting that the system was driven beyond the optimum degree

of oxidation. Nevertheless, the observed changes do not preclude the possibility of forming vivianite during the process. Unravelling the mechanistic processes during microaeration is important for identifying optimal windows to promote phosphorus removal from solution and, perhaps, vivianite formation, while avoiding excessive iron oxidation.

To interpret the aeration response of the initial sludge sample, two mechanistic scenarios were developed based on the combined observations (Table 3; Fig. 6). These observations include: (i) the release of sulphur to solution with delayed sulphate formation under low ORP conditions (−220 and −150 mV; section 3.1), (ii) a pronounced decrease in dissolved phosphorus due to adsorption or precipitation (section 3.1), and (iii) the presence of a magnetically split Fe(II)/Fe(III) Mössbauer component at 20 K exclusively in the initial sample.

Scenario A – Coupled Fe–S Oxidation: In this scenario, iron and sulphur oxidation processes proceed together. Surface oxidation of FeS_x leads to sulphide dissolution, explaining the increase in dissolved sulphur and the initially delayed formation of sulphate. The lag in sulphate formation can be attributed to transient elemental sulphur, which is commonly produced during early-stage oxidation of sulphides (section 3.1). The transient rise in soluble Fe during the first 48 h (Fig. 3) is consistent with FeS_x dissolution expected under early microaeration. In consequence, the decrease in dissolved phosphorus is consistent with Fe losing sulphide as its primary ligand and binding phosphorus, and after prolonged aeration, the formation of Fe(III) hydroxyphosphates or ferric oxyhydroxides that adsorb phosphate. The 20 K Fe(II)/Fe(III) Mössbauer component may correspond to a weakly ordered FeS_x phase, although the fit uncertainty makes precise comparison to literature challenging. Meanwhile, the persistent pm ls Fe(II) signal at 4 K likely represents a more stable FeS_x species, such as pyrite. Previous work has shown that iron sulphide oxidation at near-neutral pH can yield lepidocrocite, elemental sulphur, and sulphate (Wang et al., 2023). Moreover, the formation of passivating surface layers may shield remaining FeS_x from complete oxidation (Jeong et al., 2010). Overall, Scenario A suggests that labile FeS_x phases undergo surface oxidation to form Fe(III) oxyhydroxides capable of binding phosphorus, while sulphide is released and ultimately oxidized to sulphate.

Scenario B – Decoupled Fe and S Oxidation: In the alternative scenario, iron and sulphur oxidation proceed independently. If part of the sulphur pool existed as solid elemental sulphur, its oxidation during aeration would explain the observed sulphur release; however, it would not account for the initially low sulphate concentrations. Phosphorus removal would then be less directly linked to sulphide dissolution. Instead, aeration may shift carbonate equilibria through CO_2 stripping, destabilizing ferrous carbonate or green rust phases and thereby promoting phosphate precipitation or adsorption onto newly formed Fe(III) oxyhydroxides—similar to the outcome of Scenario A, but driven by different mechanisms. The indications of green rust in the Mössbauer spectra (section 3.2, Text A 1) are also consistent with this scenario, and phosphate adsorption on green rust has been demonstrated (Kubeneck et al., 2024, 2025). A mass-balance consideration further supports the presence of multiple sulphur pools: the ≈10% persistent pm ls Fe(II)/Fe(III) signal at 4 K corresponds to roughly 60 mmol Fe g^{-1} DW. If this were entirely pyrite (Fe/S = 0.5), it would imply ~130 mmol S g^{-1} DW—representing only about one-third of the total sulphur. If the magnetically distributed species observed by Mössbauer spectroscopy in the initial sample is indeed FeS_x, this would account for another 40% of the sulphur, at a Fe/S = 1. The remaining 30% sulphur could therefore be present as organic sulphur or elemental sulphur. In literature, only ~40% of sulphur was found as FeS_x-bound, with ~30% present as reduced organic sulphur and ~20% as elemental sulphur (Shakeri Yekta et al., 2014). Moreover, elevated Fe/S ratios, such as in the digested sludge used in this sample, are also known to favour polysulphide and elemental sulphur formation (Sand et al., 2001). Yet, elemental sulphur was not detected with SEM-EDX analysis of anaerobically dried samples, but this may reflect small particle size—typically 1–20 μm in biological desulphurization (Mol et al., 2020, 2021), or even nanoparticulate forms in natural waters (Findlay et al., 2014)—or sample-preparation artifacts that could lead to iron sulphide oxidation (Wilfert et al., 2018, section 3.2). In summary, Scenario B suggests that elemental sulphur was solubilized and oxidized during microaeration, while iron phases such as green rust exchanged ligands or were oxidized, enhancing their ability to bind phosphate.

In summary, Scenario A, involving FeS_x dissolution, provides a plausible explanation for the disappearance of the magnetically distributed species in the 20 K Mössbauer spectra upon aeration, as well as the absence of sulphate formation during the initial stage of microaeration. In contrast, Scenario B is consistent with the extensive oxidation of both iron and sulphur species observed at the end of the experiments. Together, these observations suggest that the early stages of microaeration may be dominated by the processes described in Scenario A, whereas continued aeration progressively shifts the system towards the oxidation pathways described in Scenario B. While both scenarios are consistent with the experimental observations, their contributions require further mechanistic validation. Such validation would benefit from experiments in well-defined Fe/S/P systems using ultrapure water. However, reproducing representative FeS phases remains challenging due to their rapid transformation, and the complexity of digested sludge makes it difficult to mimic their native speciation under controlled conditions. Addressing these challenges would provide valuable fundamental insight into iron sulphide transformations and improve the mechanistic understanding of phosphorus recovery processes. From a process perspective, the findings suggest that optimization should focus on preserving reactive Fe(II) and limiting extensive surface oxidation during the initial stages of microaeration, thereby maximizing the time window in which vivianite precipitation and elemental sulphur formation can occur before continued oxidation converts Fe(II) to Fe(III) and elemental sulphur to sulphate.

Table 3
Comparison of Scenario A (Surface oxidation combined with iron sulphide dissolution) and Scenario B (Elemental sulphur oxidation and iron(II) compound oxidation) on their potential to match the observations.

Observation	Scenario A	Scenario B
	Sulphide oxidation	Elemental sulphur oxidation
Sulphur release	x	x
Delayed sulphate release	x	
	Surface oxidation of iron(II) sulphide to iron(III) oxyhydroxydes	Destruction of other iron(II)/(III) binding
Phosphate adsorption/ binding	x	x
Magnetically distributed species	x	

3.4. Opportunities and limitations of microaeration for phosphorus recovery in digested sludge

.

Although microaeration did not enhance vivianite formation, it did promote substantial phosphate precipitation, which is relevant for wastewater treatment applications. Lower dissolved phosphate concentrations reduce the demand for iron coagulants typically required for further phosphate removal. However, aeration is not the only oxidative strategy capable of generating this effect. Previous studies by Ismail et al. (2022) and Yin et al. (2021) evaluated the ability of several oxidants, including hydrogen peroxide (H_2O_2) and chlorine dioxide (ClO_2), to oxidize iron sulphides and thereby induce phosphate precipitation. Their findings are compared with those of the present study in Table 4. Among the tested oxidants, H_2O_2 was the most effective: Yin et al.

Table 4
Comparison of phosphorus precipitation and presumed iron sulphide destruction by oxidizing agents, in literature and in this study.

matrix	oxidizing agent	dose	soluble P start (mM)	P precipitated (%)	FeS_x start (mM)	FeS_x reduction (%)	S product	study
liquid sludge bottom sedimentation tank	H_2O_2	500 mg/L	3.1	58	2.0	17-84	SO_4^{2-}/ SO_3^{2-}/S^0	Yin et al., 2021
liquid sludge bottom sedimentation tank	ClO_2	400 mg/L	3.1	94	2.0	0-26	SO_4^{2-}/SO_3^{2-}	Yin et al., 2021
spiked raw filtered wastewater	H_2O_2	300 mg/L	16.1	32	5.1	100	S^0	Ismail et al., 2022
digsted sludge NW to −220 mV	air	1 L/min + CO_2	3.7	76	9	58	SO_4^{2-}/?	this study

(2021) reported that 500 mg L^{-1} H_2O_2 removed up to 90% of phosphate, and Ismail et al. (2022) observed maximum FeS_x oxidation at 300 mg L^{-1} H_2O_2 with a corresponding $\Delta S/\Delta P$ ratio of 1. In the aeration experiments of the present study, phosphate removal was slightly lower but exceeded that observed with ClO_2. This comparison is of practical interest because ClO_2 appears to be a milder oxidant toward iron, potentially preserving Fe(II) and thereby favouring vivianite formation.

Quantifying iron sulphide oxidation in sludge solids remains challenging. Yin et al. (2021) and Ismail et al. (2022) used Fe(II) oxidation as an indirect proxy for FeS_x destruction; however, oxidized iron in their systems may not have originated exclusively from FeS_x. In our study, solid-phase sulphur loss between the initial and −220 mV samples was used as an indicator (Text A 2, Table A 2), though it remains uncertain whether this sulphur originated from FeS_x or other sulphur pools. Compared with aeration, H_2O_2 induced more extensive iron sulphide oxidation and produced elemental sulphur, a valuable product for sulphur recovery (de Sousa et al., 2017). Nevertheless, aeration presents an alternative for sulphur oxidation and phosphate removal, though its performance requires further optimization.

Future optimization should focus on enhancing phosphate precipitation. Promoting elemental sulphur and vivianite formation also remains attractive because vivianite binds more phosphorus per mole of iron (Fe/P = 1.5), and the products are interesting for recovery. One possible strategy is to refine aeration duration: after 24–48 h, phosphorus removal plateaued, likely due to excessive Fe(III) formation. Transitioning to anaerobic incubation after this point could promote vivianite formation if vivianite nucleates more rapidly than FeS_x (Roussel and Carliell-Marquet, 2016). A systematic investigation of ORP, pH, and the interplay between aeration and anaerobic conditions is needed. Finally, experiments combining ultrapure water and digested sludge supernatant could provide valuable insight into the mineral transformation pathways. Comprehensive solid-phase characterization using Mössbauer spectroscopy, sulphur extractions, and X-ray absorption spectroscopy (XAS) (Shakeri Yekta et al., 2014) may further elucidate the coupled evolution of iron, phosphorus, and sulphur.

4. Conclusion

This study provides mechanistic insight into the Fe–S–P transformations that govern the response of digested sludge to controlled microaeration,. ORP-controlled microaeration was evaluated as a strategy to selectively oxidize reactive iron sulphides while preserving sufficient Fe(II) for vivianite-based phosphorus recovery. Although microaeration resulted in the anticipated increase in dissolved sulphur species and decrease in soluble phosphorus, the applied aeration conditions ultimately promoted oxidation of existing vivianite rather than net vivianite formation. Yet, increasing the redox potential to −220 mV was sufficient to achieve phosphate removal, especially in the first 48 h of aeration.

Further optimization of aeration time and intensity may help exploit the early stage of microaeration while avoiding excessive oxidation. Such optimization could improve phosphorus recovery, reduce iron coagulant demand, and potentially enable combined recovery of phosphorus and sulphur from digested sludge. At the same time, further fundamental research is needed to better understand iron sulphide speciation and transformations in both simplified Fe/S/P systems and complex sludge matrices.

Declaration of generative AI and AI-assisted technologies in the writing process

During the preparation of this work the author(s) used Microsoft Copilot in order to improve the writing style. After using this tool, the authors reviewed and edited the content as needed and take full responsibility for the content of the published article.

CRediT authorship contribution statement

Sophie Banke: Conceptualization, Data curation, Formal analysis, Investigation, Methodology, Visualization, Writing – original draft, Writing – review & editing. **Femke Deelstra:** Data curation, Formal analysis. **Thomas Prot:** Conceptualization, Supervision, Writing – review & editing. **Leon Korving:** Conceptualization, Supervision, Writing – review & editing. **Carlo Belloni:** Formal analysis, Writing – review & editing. **Iulian A. Dugulan:** Formal analysis, Writing – review & editing. **Mark C.M. van Loosdrecht:** Conceptualization, Supervision, Writing – review & editing.

Declaration of competing interest

The authors declare that they have no known competing financial interests or personal relationships that could have appeared to influence the work reported in this paper.

Acknowledgment

This work was performed in the cooperation framework of Wetsus, European Centre of Excellence for Sustainable Water Technology (www.wetsus.nl). Wetsus is co-funded by the European Union (Horizon Europe, LIFE, Interreg and EDRF), the Province of Fryslân and the Dutch Government: Ministry of Economic Affairs (TTT, SBO & PPS-I/TKI Water Technology), Ministry of Education, Culture and Science (TTT & SBO) and Ministry of Infrastructure and Water Management (National Growth Fund - UPPWATER). This project has received funding from the European Union's Horizon 2020 research and innovation programme under the Marie Skłodowska-Curie grant agreement No 956454 (RecaP). The authors would like to thank the participants of the research theme "Phosphate recovery" for the fruitful discussions and their financial support. Ruud Hendrikx at the Department of Materials Science and Engineering of the Delft University of Technology is acknowledged for the X-ray analysis. The authors thank Andries Tuinhof for constructing the reactor, and Sam Rutten and Kestral Johnston for their input on ORP control and sulphur speciation.

Appendix A. Supplementary data

Supplementary data to this article can be found online at https://doi.org/10.1016/j.apgeochem.2026.107025.

Data availability

Data will be made available on request.

References

Amin, L., Al-Juboori, R.A., Lindroos, F., Bounouba, M., Blomberg, K., Viveros, M.L., Graan, M., Azimi, S., Lindén, J., Mikola, A., Spérandio, M., 2024. Tracking the formation potential of vivianite within the treatment train of full-scale wastewater treatment plants. Sci. Total Environ. 912, 169520. https://doi.org/10.1016/j.scitotenv.2023.169520.

Cao, J., Wu, Y., Zhao, J., Jin, S., Aleem, M., Zhang, Q., Fang, F., Xue, Z., Luo, J., 2019. Phosphorus recovery as vivianite from waste activated sludge via optimizing iron source and pH value during anaerobic fermentation. Bioresour. Technol. 293, 122088. https://doi.org/10.1016/j.biortech.2019.122088.

Chen, Q., Wu, W., Qi, D., Ding, Y., Zhao, Z., 2020. Review on microaeration-based anaerobic digestion: state of the art, challenges, and prospectives. Sci. Total Environ. 710, 136388. https://doi.org/10.1016/j.scitotenv.2019.136388.

Chen, X., Zheng, M., Cheng, X., Wang, C., Xu, K., 2022. Impact of impurities on vivianite crystallization for phosphate recovery from process water of hydrothermal carbonization of kitchen waste. Resour. Conserv. Recycl. 185, 106438. https://doi.org/10.1016/j.resconrec.2022.106438.

Claff, S.R., Sullivan, L.A., Burton, E.D., Bush, R.T., 2010. A sequential extraction procedure for acid sulfate soils: partitioning of iron. Geoderma 155, 224–230. https://doi.org/10.1016/j.geoderma.2009.12.002.

de Sousa, J.T., Lima, J. de F., da Silva, V.C., Leite, V.D., Lopes, W.S., 2017. Recovery of elemental sulphur from anaerobic effluents through the biological oxidation of sulphides. Environ. Technol. 38, 529–537. https://doi.org/10.1080/09593330.2016.1201148.

Dyar, M.D., Jawin, E.R., Breves, E., Marchand, G., Nelms, M., Lane, M.D., Mertzman, S. A., Bish, D.L., Bishop, J.L., 2014. Mossbauer parameters of iron in phosphate minerals: implications for interpretation of martian data. Am. Mineral. 99, 914–942. https://doi.org/10.2138/am.2014.4701.

Findlay, A.J., Gartman, A., MacDonald, D.J., Hanson, T.E., Shaw, T.J., Luther, G.W., 2014. Distribution and size fractionation of elemental sulfur in aqueous environments: the Chesapeake Bay and Mid-Atlantic Ridge. Geochem. Cosmochim. Acta 142, 334–348. https://doi.org/10.1016/j.gca.2014.07.032.

Grodzicki, M., Amthauer, G., 2000. Electronic and magnetic structure of vivianite: cluster molecular orbital calculations. Phys. Chem. Miner. 27, 694–702. https://doi.org/10.1007/s002690000125.

Hu, Y., Wu, G., Li, R., Xiao, L., Zhan, X., 2020. Iron sulphides mediated autotrophic denitrification: an emerging bioprocess for nitrate pollution mitigation and sustainable wastewater treatment. Water Res. 179, 115914. https://doi.org/10.1016/j.watres.2020.115914.

Ismail, A., Jang, E., Schraa, O., Walton, J.R., Zamanzadeh, M., Elbeshbishy, E., Santoro, D., 2022. Model-based investigation of the chemical phosphorus removal potential of the peroxide regenerated iron-sulfide control technology. Water Environ. Res. 94. https://doi.org/10.1002/wer.10754.

Jeong, H.Y., Han, Y.-S., Park, S.W., Hayes, K.F., 2010. Aerobic oxidation of mackinawite (FeS) and its environmental implication for arsenic mobilization. Geochem. Cosmochim. Acta 74, 3182–3198. https://doi.org/10.1016/j.gca.2010.03.012.

Kirk Nordstrom, D., 1982. Aqueous pyrite oxidation and the consequent formation of secondary iron minerals, 37–56. https://doi.org/10.2136/sssaspecpub10.c3.

Klencsár, Z., Kuzmann, E., Vértes, A., 1996. User-friendly software for Mössbauer spectrum analysis. J. Radioanal. Nucl. Chem. Art. 210, 105–118. https://doi.org/10.1007/BF02055410.

Krayzelova, L., Bartacek, J., Díaz, I., Jeison, D., Volcke, E.I.P., Jenicek, P., 2015. Microaeration for hydrogen sulfide removal during anaerobic treatment: a review. Rev. Environ. Sci. Biotechnol. 14, 703–725. https://doi.org/10.1007/s11157-015-9386-2.

Kubeneck, L.J., Notini, L., Rothwell, K.A., Fantappiè, G., Huthwelker, T., ThomasArrigo, L.K., Kretzschmar, R., 2024. Transformation of vivianite in intertidal sediments with contrasting sulfide conditions. Geochem. Cosmochim. Acta 370, 173–187. https://doi.org/10.1016/j.gca.2024.01.020.

Kubeneck, L.J., Rothwell, K.A., Notini, L., ThomasArrigo, L.K., Schulz, K., Fantappiè, G., Joshi, P., Huthwelker, T., Kretzschmar, R., 2025. In situ vivianite formation in intertidal sediments: ferrihydrite-adsorbed P triggers vivianite formation. Environ. Sci. Technol. 59, 523–532. https://doi.org/10.1021/acs.est.4c10710.

Kubeneck, L.J., ThomasArrigo, L.K., Rothwell, K.A., Kaegi, R., Kretzschmar, R., 2023. Competitive incorporation of Mn and Mg in vivianite at varying salinity and effects on crystal structure and morphology. Geochem. Cosmochim. Acta 346. https://doi.org/10.1016/j.gca.2023.01.029.

Lan, Y., Butler, E.C., 2014. Monitoring the transformation of mackinawite to greigite and pyrite on polymer supports. Appl. Geochem. 50, 1–6. https://doi.org/10.1016/j.apgeochem.2014.07.020.

Liu, J., Izon, G., Wang, J., Antler, G., Wang, Z., Zhao, J., Egger, M., 2018. Vivianite formation in methane-rich deep-sea sediments from the South China Sea. Biogeosciences 15, 6329–6348. https://doi.org/10.5194/bg-15-6329-2018.

Ma, M., Overvest, P., Hijlkema, A., Mangold, S., McCammon, C., Voegelin, A., Behrends, T., 2023. Phosphate burial in aquatic sediments: rates and mechanisms of vivianite formation from mackinawite. Chem. Eng. J. Adv. 16, 100565. https://doi.org/10.1016/j.ceja.2023.100565.

Meijer, H.C., Van den Handel, J., Frikkee, E., 1967. Magnetic behaviour of vivianite, Fe3(PO4)2.8H2O. Physica 34, 475–483. https://doi.org/10.1016/0031-8914(67)90015-8.

Mejia Likosova, E., Keller, J., Rozendal, R.A., Poussade, Y., Freguia, S., 2013. Understanding colloidal FeS formation from iron phosphate precipitation sludge for optimal phosphorus recovery. J. Colloid Interface Sci. 403, 16–21. https://doi.org/10.1016/j.jcis.2013.04.001.

Mol, A., van der Weijden, R., Klok, J., Buisman, C., 2020. Properties of sulfur particles formed in biodesulfurization of biogas. Minerals 10, 433. https://doi.org/10.3390/min10050433.

Mol, A.R., Meuwissen, D.J.M., Pruim, S.D., Zhou, C., van Vught, V., Klok, J.B.M., Buisman, C.J.N., van der Weijden, R.D., 2021. Novel agglomeration strategy for elemental sulfur produced during biological gas desulfurization. ACS Omega 6, 27913–27923. https://doi.org/10.1021/acsomega.1c03701.

Moses, C.O., Herman, J.S., 1991. Pyrite oxidation at circumneutral pH. Geochem. Cosmochim. Acta 55, 471–482. https://doi.org/10.1016/0016-7037(91)90005-P.

Murad, E., Cashion, J., 2004. Mössbauer Spectroscopy of Environmental Materials and Their Industrial Utilization. Springer Science & Business Media.

Nguyen, H., Prot, T., Wijdeveld, W., Korving, L., Dugulan, A.I., Brück, E., Haarala, A., van Loosdrecht, M.C.M., 2024. Robust magnetic vivianite recovery from digested sewage sludge: evaluating resilience to sludge dry matter and particle size variations. Water Res. 266, 122407. https://doi.org/10.1016/j.watres.2024.122407.

Nielsen, A.H., Vollertsen, J., Hvitved-Jacobsen, T., 2006. Kinetics and stoichiometry of aerobic sulfide oxidation in wastewater from sewers—effects of pH and temperature. Water Environ. Res. 78, 275–283. https://doi.org/10.2175/106143005X94367.

Notini, L., Schulz, K., Kubeneck, L.J., Grigg, A.R.C., Rothwell, K.A., Fantappiè, G., ThomasArrigo, L.K., Kretzschmar, R., 2023. A new approach for investigating iron mineral transformations in soils and sediments using ^{57} Fe-Labeled minerals and ^{57} Fe Mössbauer spectroscopy. Environ. Sci. Technol. 57, 10008–10018. https://doi.org/10.1021/acs.est.3c00434.

Nriagu, J.O., 1972. Stability of vivianite and ion-pair formation in the system fe3(PO4)2-H3PO4H3PO4-H2o. Geochem. Cosmochim. Acta 36, 459–470. https://doi.org/10.1016/0016-7037(72)90035-X.

Prot, T., Wijdeveld, W., Eshun, L.E., Dugulan, A.I., Goubitz, K., Korving, L., Van Loosdrecht, M.C.M., 2020. Full-scale increased iron dosage to stimulate the formation of vivianite and its recovery from digested sewage sludge. Water Res. 182. https://doi.org/10.1016/j.watres.2020.115911.

Rickard, D., Griffith, A., Oldroyd, A., Butler, I.B., Lopez-Capel, E., Manning, D.A.C., Apperley, D.C., 2006. The composition of nanoparticulate mackinawite, tetragonal iron(II) monosulfide. Chem. Geol. 235, 286–298. https://doi.org/10.1016/j.chemgeo.2006.07.004.

Rothe, M., Kleeberg, A., Grüneberg, B., Friese, K., Pérez-Mayo, M., Hupfer, M., 2015. Sedimentary sulphur:iron ratio indicates vivianite occurrence: a study from two contrasting freshwater systems. PLoS One 10, e0143737. https://doi.org/10.1371/journal.pone.0143737.

Roussel, J., Carliell-Marquet, C., 2016. Significance of vivianite precipitation on the mobility of iron in anaerobically digested sludge. Front. Environ. Sci. 4. https://doi.org/10.3389/fenvs.2016.00060.

Sand, W., Gehrke, T., Jozsa, P.-G., Schippers, A., 2001. (Bio)chemistry of bacterial leaching—direct vs. indirect bioleaching. Hydrometallurgy 59, 159–175. https://doi.org/10.1016/S0304-386X(00)00180-8.

Shakeri Yekta, S., Svensson, B.H., Björn, A., Skyllberg, U., 2014. Thermodynamic modeling of iron and trace metal solubility and speciation under sulfidic and ferruginous conditions in full scale continuous stirred tank biogas reactors. Appl. Geochem. 47, 61–73. https://doi.org/10.1016/j.apgeochem.2014.05.001.

Thompson, A., Byrne, J.M., Dreher, C.L., Grigg, A.R.C., Joshi, P., Latta, D.E., Neumann, A., Notini, L., O'Neill, K.E.B., Rothwell, K.A., 2025. Current practices for analyzing soils and sediments via Mössbauer spectroscopy. J. Plant Nutr. Soil Sci. 188, 742–773. https://doi.org/10.1002/jpln.12024.

van der Grift, B., Behrends, T., Osté, L.A., Schot, P.P., Wassen, M.J., Griffioen, J., 2016. Fe hydroxyphosphate precipitation and Fe(II) oxidation kinetics upon aeration of Fe (II) and phosphate-containing synthetic and natural solutions. Geochem. Cosmochim. Acta 186, 71–90. https://doi.org/10.1016/j.gca.2016.04.035.

Wang, H., Zhu, J., Fu, Q.-L., Xiong, J.-W., Hong, C., Hu, H.-Q., Violante, A., 2015. Adsorption of phosphate onto Ferrihydrite and Ferrihydrite-Humic acid complexes. Pedosphere 25, 405–414. https://doi.org/10.1016/S1002-0160(15)30008-4.

Wang, T., Liu, Y., Liu, B., 2023. The pH-sensitive oxygenation of FeS: mineral transformation and immobilization of Cr(VI). Water Res. 233, 119722. https://doi.org/10.1016/j.watres.2023.119722.

Wijdeveld, W.K., Prot, T., Sudintas, G., Kuntke, P., Korving, L., van Loosdrecht, M.C.M., 2022. Pilot-scale magnetic recovery of vivianite from digested sewage sludge. Water Res. 212. https://doi.org/10.1016/j.watres.2022.118131.

Wilfert, P., Dugulan, A.I., Goubitz, K., Korving, L., Witkamp, G.J., Van Loosdrecht, M.C. M., 2018. Vivianite as the main phosphate mineral in digested sewage sludge and its role for phosphate recovery. Water Res. 144. https://doi.org/10.1016/j.watres.2018.07.020.

Wilfert, P., Kumar, P.S., Korving, L., Witkamp, G.-J., van Loosdrecht, M.C.M., 2015. The relevance of phosphorus and iron chemistry to the recovery of phosphorus from

wastewater: a review. Environ. Sci. Technol. 49, 9400–9414. https://doi.org/10.1021/acs.est.5b00150.

Wilfert, P., Mandalidis, A., Dugulan, A.I., Goubitz, K., Korving, L., Temmink, H., Witkamp, G.J., Van Loosdrecht, M.C.M., 2016. Vivianite as an important iron phosphate precipitate in sewage treatment plants. Water Res. 104, 449–460. https://doi.org/10.1016/j.watres.2016.08.032.

Yin, R., Peng, J., Sun, J., Li, C., Xia, D., Shang, C., 2021. Simultaneous removal of hydrogen sulfide, phosphate and emerging organic contaminants, and improvement of sludge dewaterability by oxidant dosing in sulfide-iron-laden sludge. Water Res. 203, 117557. https://doi.org/10.1016/j.watres.2021.117557.